PAPER

Check for updates

Enhanced electrocatalytic hydrogen evolution by molybdenum disulfide nanodots anchored on MXene under alkaline conditions†

Xiaoyu Wang,‡[a] Wenbin You,‡[b] Liting Yang,[b] Guanyu Chen,[b] Zhengchen Wu,[b] Chang Zhang,[b] Qianjin Chen [ID] *[a] and Renchao Che [ID] *[bc]

Efficient hydrogen production through electrocatalysis represents a promising path for the future clean energy. Molybdenum disulfide (MoS_2) is a good substitute for platinum-based catalysts, due to its low cost and high activity. However, the limited active sites and low electrical conductivity of MoS_2 hinder its large-scale industrial application under alkaline conditions. Herein, we constructed MoS_2 nanodots anchored on an MXene/nickel foam (MoS_2 NDs/MXene/NF) heterostructure by a cascade polymerization synthesis and *in situ* vulcanization. The prepared heterostructure displays an ultralow overpotential of 94 mV at a current density of 10 mA cm^{-2} with a Tafel slope of only 59 mV dec^{-1} in alkaline (1 M KOH) hydrogen evolution reaction (HER), and is better than conventional MoS_2 electrocatalysts reported so far. Fine structural analysis indicates that MoS_2 NDs are dispersed uniformly on the surface of the heterostructure with consistent orientation, leading to the improvement of MoS_2 conductivity with more paths for electron transfer. Moreover, the orientation of the synthesized MoS_2 NDs was verified to expose the more (002) crystal plane, which exhibits higher activity than other planes. Our results demonstrate that MoS_2 NDs with heterostructure design and preferential growth can serve as high-efficiency noble-metal free electrocatalysts for the HER in alkaline solution.

Introduction

Hydrogen energy is deemed a promising alternative to fossil fuels, due to its features of high energy capacity and environmental friendliness.[1–3] The efficient and economical way of hydrogen production from electrochemical water splitting is a long-standing goal for the energy crisis solution.[4–6] Despite the HER being easier under acidic conditions, accompanying corrosion of electrolytic equipment and destruction of catalysts become a huge bottleneck for its industrial application.[7] Instead, alkaline electrolysis, due to the long durability of the electrolyzer, the high reliability of the production process, and the long life of the catalyst, has attracted tremendous attention in the past decade.[8] Platinum and its derivatives till now are still the most common HER catalysts, both under acidic and alkaline conditions.[9,10] Considering the scarcity of noble-metal catalysts, the development of sustainable catalysts with low cost and abundance has been the focus of intensive research efforts.[11]

The concentration of hydrogen ions in alkaline medium is ~8 to 14 orders of magnitude lower than that in acidic medium, resulting in the drawbacks of sluggish water adsorption and poor dissociation dynamics during water splitting. Thus, greater efforts on increasing the accessibility of active sites and surface modification with water adsorption components have been adopted to develop high-performance alkaline HER electrocatalysts.[11–14] Recently, non-precious Mo-based materials have been proved experimentally to replace platinum and its derivatives,[11,12] because of the lower Gibbs-energy of hydrogen adsorption analogous to platinum. Typically, MoS_2 with a two-dimensional layered nanostructure, recognized as the most important one, shows catalytic sites at its layer edges during the Volmer reaction.[15–19] The vertical growth of MoS_2 on a flat substrate or nanowire surfaces can expose more edge sites.[20,21] Meanwhile, MoS_2 nanosheets, even ultrasmall nanodots, are preferable because the accompanying higher specific surface area and more edge atoms strikingly boost the HER catalytic activity.[22–24] Worse still, the nanostructures tend to agglomerate after being formed into electrodes, which hinders sustainable electrocatalytic activity, thus far from being satisfactory for practical electrolysis.[25,26] As for surface modification to enhance the catalyst hydrophilicity and cleave the HO–H bond, nano-assembly hierarchical structures, such as MoS_2-Ni/Co

[a]State Key Laboratory for Modification of Chemical Fibers and Polymer Materials, College of Chemistry, Chemical Engineering and Biotechnology, Donghua University, Shanghai, 201620, P. R. China. E-mail: qianjinchen@dhu.edu.cn

[b]Laboratory of Advanced Materials, Shanghai Key Lab of Molecular Catalysis and Innovative Materials, Department of Materials Science, Fudan University, Shanghai 200438, P. R. China. E-mail: rcche@fudan.edu.cn

[c]Joint-Research Center for Computational Materials, Zhejiang Laboratory, Hangzhou 311100, P. R. China

† Electronic supplementary information (ESI) available. See https://doi.org/10.1039/d2na00376g

‡ These authors contributed equally to this work.

compounds with porous media,[14] have been constructed and used as highly efficient electrocatalysts. However, the even worse conductivity of Ni/Co compounds, such as hydroxide, sulfide, and phosphide, causes more energy waste in hydrogen production.

The electrical conductivity enhancement of electrocatalysts can simultaneously accelerate the reaction rate and reduce overpotentials. Due to the semiconducting properties of molybdenum disulfide, a minimized bandgap means less difficulty for carrier migration. Nevertheless, the bulk form of MoS_2 tends to have a smaller bandgap (1.2 eV) than that of few-layer MoS_2 (1.9 eV for monolayer MoS_2). In another word, the MoS_2 nanosheets or nanodots possess poor electrical conductivity. Thus, defect engineering strategies, such as introducing holes, cracks, and crimps, have been extensively developed and utilized to minimize the bandgap, and achieve higher active site exposure[22,27] at the same time. However, most defects influence slightly the intrinsic property regulation of MoS_2. In this context, introducing a highly conductive substrate could simultaneously optimize the HER performance of MoS_2 nanosheets or nanodots. Of all substrates, the $Ti_3C_2T_x$ MXene shows great promise due to its good hydrophilicity and metallic conductivity (up to 10 000 S cm^{-1}), having been applied in supercapacitors, water treatment, microwave absorption,[28] and electromagnetic interference shielding.[10] The structure design between MXene and MoS_2 is assumed to improve the conductivity of the electrocatalyst and deliver enough activity toward the HER, while the remaining challenges of uniform dispersion of catalytically active sites and effective protection of the MXene conductive substrate from surface oxidization and anti-aggregation should be overcome first.[16,20,29]

Motivated by the above considerations, we developed an MXene/NF substrate with preferential growth MoS_2 nanodots (MoS_2/MXene/NF), of which the more active edge exposure enhances the HER performance. Notably, the chelated molybdate ions and $Ti_3C_2T_x$ MXene flakes encapsulated by polydopamine (PDA), used as a precursor, provide uniformly dispersed MoS_2 nanodots anchored on MXene with ultra-small size and inhibit surface oxidation of MXenes during annealing and sulfurization treatment.[30] The synthesized MoS_2/MXene heterostructure, confirmed by morphology, structure, phase, and elemental chemical valence characterization, displays a synergistic effect of active MoS_2 nanodots and conductive $Ti_3C_2T_x$ MXene flakes for fast charge transfer. The optimal MoS_2/MXene/NF yields remarkable HER activities with a Tafel slope of 59 mV dec^{-1} and an overpotential of 94 mV at 10 mA cm^{-2}. Due to its excellent stability over 2000 cycles of cyclic voltammetry tests in an alkaline electrolyte, MoS_2/MXene/NF has been certified superior to most non-noble metal catalysts in alkaline solution. This work sheds new insight into nanostructure construction for Mo-based catalysts to enhance their capability of catalytic water decomposition.

Results and discussion

Fig. 1 shows the schematic illustration of a novel strategy for constructing MoS_2 NDs/MXene with abundant exposed sites grown on a 3D self-supporting electrode. First, ultrathin

MXenes were obtained by selectively etching the Al element in the MAX phase (Ti_3AlC_2) with hydrofluoric acid and the subsequent exfoliation procedure (experimental section in the ESI†). During the *in situ* polymerization process of PDA under weakly alkaline conditions, the mixture of few-layer MXenes and molybdate ions was well encapsulated on the NF substrate surface. The molybdate ions were chelated in PDA (Mo-PDA) as the precursor of MoO_3, and few-layer MXenes were fully wraped with Mo-PDA. Then, a heterostructure of $Ti_3C_2T_x$ MXene sheets decorated with MoO_3 NDs was obtained by annealing Mo-PDA/$Ti_3C_2T_x$/NF at 650 °C under a N_2 atmosphere, which inhibits the agglomeration of MoO_3 NDs and oxidation of $Ti_3C_2T_x$ due to the confinement effect of PDA. Finally, as-synthesized MoO_3 NDs/MXene was controllably sulfurized to MoS_2 NDs/MXene at sulfurization temperatures from 500 to 800 °C in a N_2 atmosphere.

The products of the schematic step are characterized by scanning electron microscopy (SEM) and transmission electron microscopy (TEM) to verify the synthetic process. The as-prepared MXene shows a layered structure in the SEM image (Fig. S1b†).[31] The clear few-layered structure of 2D MXene is further confirmed by the TEM image (Fig. S2a†). By *in situ* polymerization of dopamine, the relatively smooth surface of NF with micropores (Fig. 2a) is wrapped by a uniformly layered structure network combined with 2D MXene and Mo-PDA (Fig. S1d†). After annealing at 650 °C, the Mo-PDA transforms into MoO_3 NDs dispersed in the MXene, while the MoO_3/MXene/NF (Fig. 2b) shows a similar morphology to the Mo-PDA/MXene/NF precursor (Fig. S1d†). Moreover, the well-defined ND decorated 2D MXene structure was maintained standing on NF after the sulfurization process (Fig. 2c). The uniform distributions of MoO_3 NDs and MoS_2 NDs in carbide are more clearly seen in the TEM images (Fig. 2d and e). As for Mo-PDA/NF and its derivative MoS_2/NF (Fig. S3a–c†), a flower-like structure with about 400 nm diameter was formed on the NF surface, which is similar to the folded surface in Mo-PDA/MXene/NF (Fig. S1d†). This revealed that the $Ti_3C_2T_x$ with oxygen- or fluorine-containing terminations was identified as a charged substrate to adsorb dopamine hydrochloride chelated Mo precursors, realizing well dispersed nanostructured Mo compounds.[32–34]

The structures of MXene and its composites were further investigated by X-ray diffraction (XRD) and high-resolution TEM (HRTEM). The XRD pattern of MXenes (Fig. S2c†) shows a strong diffraction peak at 6.9°, corresponding to the typical (002) plane of $Ti_3C_2T_x$.[33,35] Meanwhile, the HRTEM image (Fig. S2b†) can also index the lattice fringes of 2D MXene. As for NF (Fig. S4†), three strong peaks located at 44.7, 52.0, and 76.5 can be well identified as Ni (JCPDS no. 04-0850). The diffraction peaks of NF didn't shift or change during the processes of *in situ* polymerization and high-temperature treatment. In addition, the (002) $Ti_3C_2T_x$ diffraction peak disappeared in the XRD pattern of MoO_3/MXene/NF and MoS_2/MXene/NF (Fig. S4†), which should be attributed to the PDA decomposition and carbon layer restacking on the surface of MXene flakes.[30,36] What's more, no obvious crystal diffraction peaks of MoO_3 and MoS_2 were found in XRD patterns with NF due to the ultra-small size of NDs and the extremely strong diffraction peak of NF.[24]
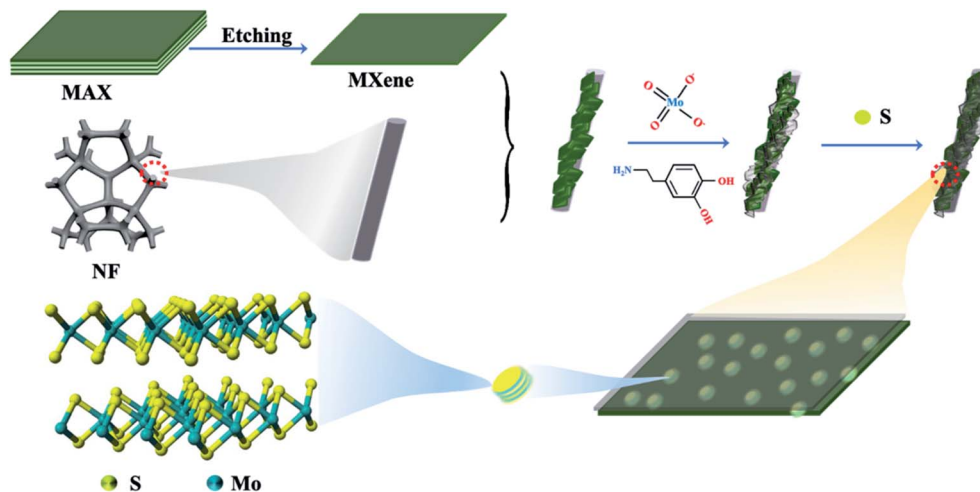
Fig. 1 Schematic diagram of the MoS$_2$ NDs/MXene/NF synthetic route.

The enlarged TEM image (Fig. 2e) exhibits ultrasmall MoO$_3$ nanodots uniformly decorated on the surface of MXene. Lattice fringes of both MoO$_3$ and MXene can be found in the HRTEM image (Fig. 2f). The carbon-coated Ti$_3$C$_2$T$_x$ MXene derived from PDA/Ti$_3$C$_2$T$_x$ retains the flat surface without the presence of TiO$_2$ species, which demonstrated that tightly covered PDA on
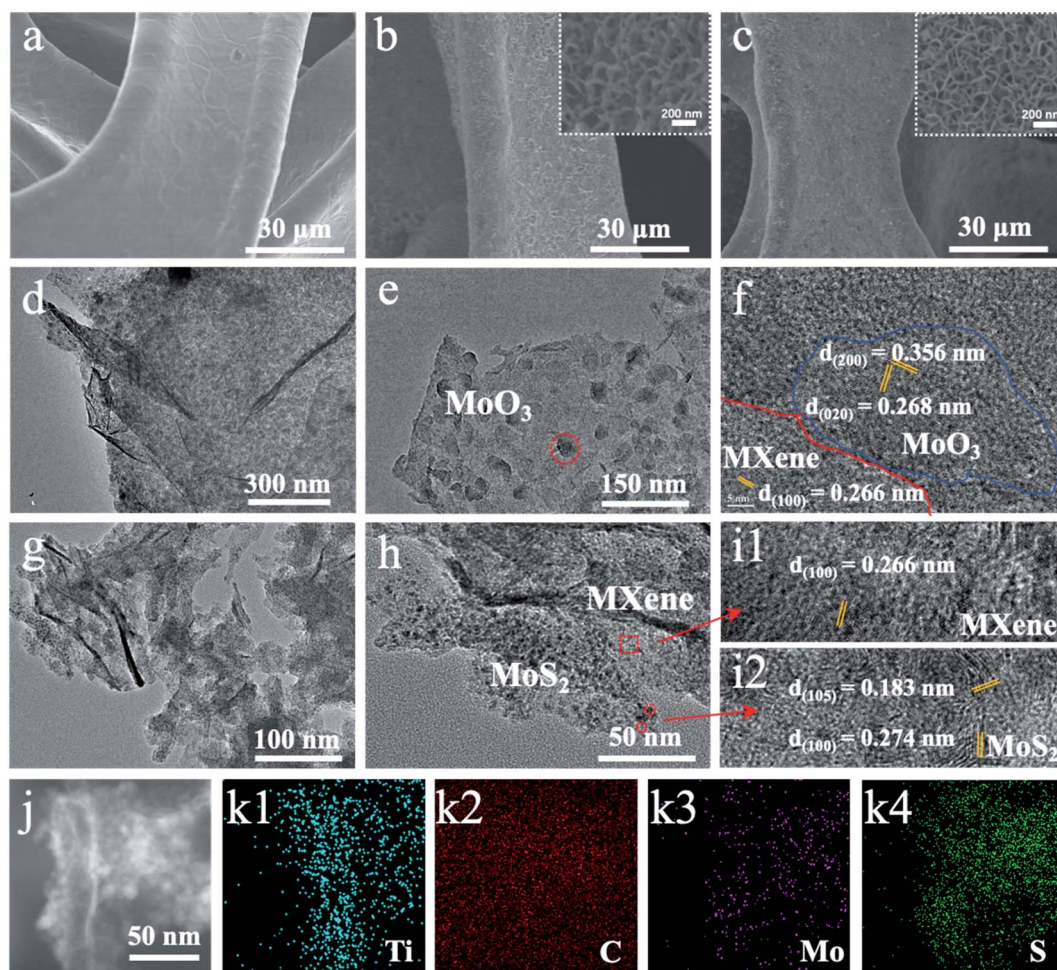

Fig. 2 SEM images of (a) NF, (b) MoO$_3$/MXene/NF, and (c) MoS$_2$/MXene/NF. The insets of (b and c) are images at high magnification. (d and e) TEM images, and (f) HRTEM image of MoO$_3$/MXene removed from MoO$_3$/MXene/NF. (g and h) TEM images, (i) HRTEM image, (j) HAADF image, and (k) EDX elemental distributions of MoS$_2$/MXene removed from MoS$_2$/MXene/NF.

the MXene surface could inhibit surface oxidation during the annealing process, to maintain excellent electrical conductivity. The morphologies of the $Ti_3C_2T_x$ MXene and molybdenum derivative are slightly changed after high-temperature sulfurization (Fig. 2g). Even smaller MoS_2 nanodots were observed on the MXene surface (Fig. 2h) after the MoO_3 vulcanization process, meaning the existence of multiple reaction points resulting in fission of MoO_3 dots at the end of the vulcanization. The corresponding HRTEM image revealed lattice fringes of 0.62 nm on the nanodot matching with the (002) plane of 2H-MoS_2 (Fig. 2i). The lattice of MoS_2 has an obvious distortion compared with MoO_3 due to the unavoidable vacancies appearing during high-temperature treatment and the two-dimensional microstructure wrinkling in MoS_2. Further analysis revealed that most of the sulfurized MoS_2 preferentially grows in the vertical direction of $Ti_3C_2T_x$ MXene flakes with (002) crystal plane exposure. The high-angle annular dark field (HAADF) image under scanning TEM mode (Fig. 2j) indicates abundant bright dots anchored on the MXene flakes. The corresponding elemental distribution images under energy-dispersive X-ray spectroscopy (EDX) show the distributions of Ti, C, Mo, and S elements (Fig. 2k), further confirming the uniform MoS_2 NDs/MXene heterostructure.

Given that EDX and HRTEM only provide foundational composition information, the X-ray photoelectron spectroscopy (XPS) analysis is further used to elucidate the electronic valence of compositions and coordination structures. Fig. S5a† shows the full spectrum of MoO_3/MXene removed from MoO_3/MXene/NF, which evidences the existence of Ti, C, Mo, O, and N. The peak of N may stem from the carbonized PDA. The signal attenuation caused by the active material package is scanned under high-resolution. By calibrating the carbon peak C (284.8 eV), +0.7 eV peak shifted, the high-resolution XPS spectrum of Mo 3d is obtained in Fig. S5b.† The peaks at 229.9, 233.2, and 236.3 eV, which can be attributed to the Mo^{4+} $3d_{5/2}$, Mo^{6+} $3d_{5/2}$, and Mo^{6+} $3d_{3/2}$, are assigned to the existence of MoO_3 after 600 °C high-temperature treatment. In addition, the deconvolution of the Ti 2p XPS spectrum (Fig. S5c†) can be fitted with TiO_2 (Ti^{4+}) Ti–X (Ti^{2+}, X = OH), Ti–C (Ti^{+}), and Ti–X (Ti^{2+}, X = F) at the peaks of 455.6, 458.4, 460.9, and 464.3 eV, respectively. Compared to the brand-new $Ti_3C_2T_x$ MXene after etching, the binding energy of Ti–C and Ti–X positively shifts,[37] revealing the obvious electron transfer from $Ti_3C_2T_x$ to MoO_3 nanodots in the heterostructure.

After further vulcanization to obtain MoS_2/$Ti_3C_2T_x$, the signal peak of sulfur can be found initially in the full spectrum peak (Fig. 3a). In the corresponding Mo 3d spectrum (Fig. 3b), the distinct peaks at 229.6 and 232.7 eV are assigned to the Mo^{4+} $3d_{5/2}$ and Mo^{4+} $3d_{3/2}$ in MoS_2, whereas the signals at 226.9 and 234.4 eV can be attributed to the S and Mo–O (MO^{6+}), respectively. The S 2p convolutional high-resolution spectrum (Fig. 3c) is divided into two peaks of S $2p_{3/2}$ and S $2p_{1/2}$ at 162.1 and 163.5 eV, revealing the −2 oxidation state of S in MoS_2. These phenomena are consistent with previous studies.[22,39] As for the Ti 2p XPS spectrum after vulcanization (Fig. 3d), similar to that of MoO_3/$Ti_3C_2T_x$, signals appear at 455.7, 459.1, 461.2, and 464.8 eV, stemming from TiO_2 (Ti^{4+}), Ti–X (Ti^{2+}, X = OH), Ti–C

(Ti^{+}), and, Ti–X (Ti^{2+}, X = F). Compared to the MoO_3 nanodots on $Ti_3C_2T_x$, the Ti–C and Ti–X binding energies of $Ti_3C_2T_x$ in the MoS_2/$Ti_3C_2T_x$ heterostructure positively shift about 0.3 eV and 0.7 eV, while the Mo^{4+} $3d_{5/2}$ peak shifts negatively from 229.9 to 229.6 eV in Mo–S. The decreasing Mo 3d binding energy and increasing Ti 2p binding energy indicate that more electrons were transferred from $Ti_3C_2T_x$ to MoS_2 nanodots. The above XPS results reveal that MoS_2 nanodots are strongly adhered to the $Ti_3C_2T_x$ MXene surface, accompanied by strong interfacial interactions existing at the $Ti_3C_2T_x$–MoS_2 heterogeneous interfaces.

To evaluate the electrocatalytic activity of MoS_2/MXene/NF towards water splitting, HER performance was investigated in a traditional three-electrode system, in which a N_2-saturated 1 M KOH solution was employed as the electrolyte. For comparison, NF, MXene/NF, and MoS_2/NF MoO_3/MXene/NF were also tested as control samples. Fig. 4a shows the steady-state linear sweep voltammograms (LSV) of the above electrodes, whose activity trend is as follows: NF < MXene/NF < MoO_3/MXene/NF < MoS_2/MXene/NF. The MXene/NF and NF show relatively worse HER activity, suggesting that both MXene and NF are not very suitable for the HER. The MoS_2/MXene/NF exhibits a low onset overpotential of 94 mV at 10 mA cm^{-2} (η_{10}) vs. reversible hydrogen electrode (RHE), which is much better than those of MoS_2/NF (η_{10} = 164 mV, Fig. S6a†), MoO_3/MXene/NF (η_{10} = 204 mV) and MXene/NF (η_{10} = 189 mV) (Fig. 4c). The Tafel slopes, as a pivotal kinetic parameter to elucidate the HER mechanism, were calculated using the Tafel equation. Here, the Tafel slope of MoS_2/MXene/NF is 59 mV dec^{-1} (Fig. 4b), and the smallest among all the compared samples.

The Tafel slope curves indicate that MoS_2/MXene/NF has extremely fast reaction kinetics. As shown in Fig. 4d and Table S1,† the comparison of HER performance between MoS_2/MXene/NF and other non-noble-metal electrocatalysts from the literature is presented.[14,23,29,35,38,39] Most of them require larger overpotentials (η_{10} over 100 mV) and higher Tafel slopes (over 60 mV dec^{-1}), which are far worse than the catalytic performance of Pt. Some non-noble metal catalysts may have a low overpotential (η_{10} < 50 mV), while their poor kinetic conditions (higher Tafel slopes exceeding 50 mV dec^{-1}) also make the performance inexhaustible. Therefore, MoS_2/MXene/NF with an ultra-low overpotential (η_{10} = 94 mV) and Tafel slope (59 mV dec^{-1}) have great potential to replace Pt in industrial applications. Meanwhile, the stability of the electrocatalyst, which is a critical indicator for catalyst practical application, has also been investigated through cyclic voltammetry (CV) cycles over 200 mV vs. RHE (Fig. 4f) and the chronoamperometry (CP) test at a constant overpotential (Fig. S7d†). The LSV curve of MoS_2/MXene/NF shows a negligible negative shift after 2000 cycles in current density compared to the initial curve. Meanwhile, the MoS_2/MXene/NF exhibits greater long-term stability, only a slight decrease over 60 000 s. SEM and XRD characterization studies of MoS_2/MXene/NF (Fig. S7a–c†) were further conducted to confirm the outstanding durability of its morphology, structure, and phase after the stability test. Similar to MoS_2/NF after electrochemical tests (Fig. S3d†), the SEM image shows that only the folded surface of the PDA
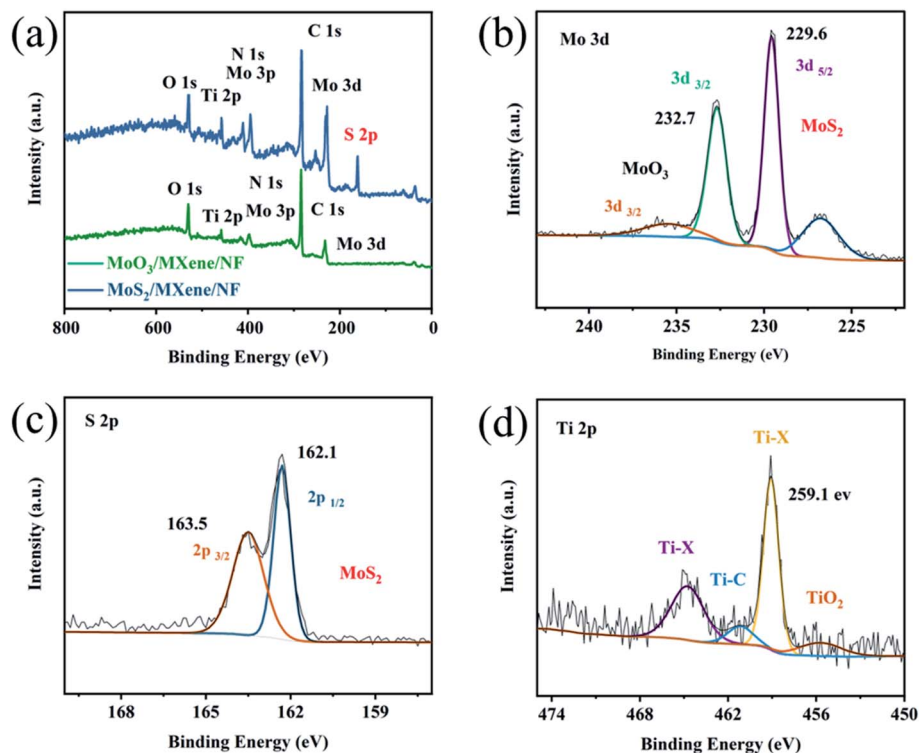
Fig. 3 (a) Full spectra of MoO₃/MXene and MoS₂/MXene removed from MoO₃/MXene/NF and MoS₂/MXene/NF. High-resolution XPS (b) Mo 3d (c) S 2p, and (d) Ti 2p spectra of MoS₂/MXene.

carbonation layer is destroyed, while the main skeleton structure and phase of MoS₂/MXene/NF remain unchanged. The excellent durability of MoS₂/MXene/NF can be attributed to the confinement effect of carbonated PDA, which protects the ion-exchange interface during the electrocatalytic process.

The above results imply that the HER activity of both $Ti_3C_2T_x$ and MoS_2 is unsatisfactory under alkaline conditions, whereas modulating the heterogeneous structure can result in an optimized HER activity. To better understand the function of the $MoS_2/Ti_3C_2T_x$ heterostructure during the HER process, the electrochemical impedance spectroscopy (EIS) measurement was performed at 200 mV vs. RHE from 10^6 Hz to 0.01 Hz. Fig. S8† displays the Nyquist plots of the above electrodes, in which the charge transfer resistance (R_{ct}) is related to the electrocatalytic kinetics at the interfaces. The MoS₂/MXene/NF delivers a much smaller R_{ct} than MoO₃/MXene/NF and MXene/NF, evidencing faster electron transfer between the MoS_2–$Ti_3C_2T_x$ heterostructure. Both the $Ti_3C_2T_x$ flake and MoS_2 nanodot contribute to the higher electrical conductivity and faster HER kinetics. Generally, the effective electrochemically active area (ECSA) is related to the electrocatalyst surface area and the number of active sites, which is estimated from the double-layer capacitance (C_{dl}) by performing cyclic voltammetry with different sweep speeds under the voltage range of the non-Faradic current (electrochemical tests). The C_{dl} value was calculated by the slope between the half capacitive current density at the median of the applied potential and the scan rates. The measured C_{dl} value for MoS₂/MXene/NF is 0.23 F

cm^{-2} (Fig. 4e and S8†), considerably better than those of MoO₃/MXene/NF (0.39 F cm^{-2}), MXene/NF (1.8 F cm^{-2}), and NF (2.6 F cm^{-2}). As the MXene/NF displays the worst ECSA, the HER active sites are assumed from the MoO_3 and MoS_2 nanodots in the heterostructure. Significantly, the ECSA of MoS₂/MXene/NF is larger than that of MoO₃/MXene/NF, indicating the extension of the electrochemical active area or the more catalytic active sites obtained after high-temperature sulfurization. Experimental studies and theoretical calculations have certified that MoS_2 active sites are mainly concentrated on the edge.[15–21] Therefore, the fixed orientation for MoS_2 NDs preferential growth on MXene flake exposes more (002) crystal planes, which exhibit more active sites for excellent HER than other planes.

Obviously, the HER performance is associated with the varied ratio of MoS₂/MXene and the construction of MoS₂–MXenes interfaces. The different ratios of MoS₂/MXene can be adjusted by c the usage of ammonium molybdate and MXene in the precursor reaction process. Though more Mo active sites are beneficial for HER performance enhancement, excessive Mo will result in larger MoS_2 dots, which have lower conductivity and a smaller percentage of active sites. What's more, a larger ratio of MoS_2 and MXene may be accompanied by the formation of MoS_2 microspheres (Fig. S3†), of which the HER performance is very poor (Fig. S6†). As for the role of the MoS₂–MXenes interface, it was known that $Ti_3C_2T_x$ itself shows negligible HER activity. So, the function of Ti-based MXenes at the interfaces is to provide a better hydrophilicity and conductivity, which will promote more efficient and direct electron transfer (Fig. 3) to
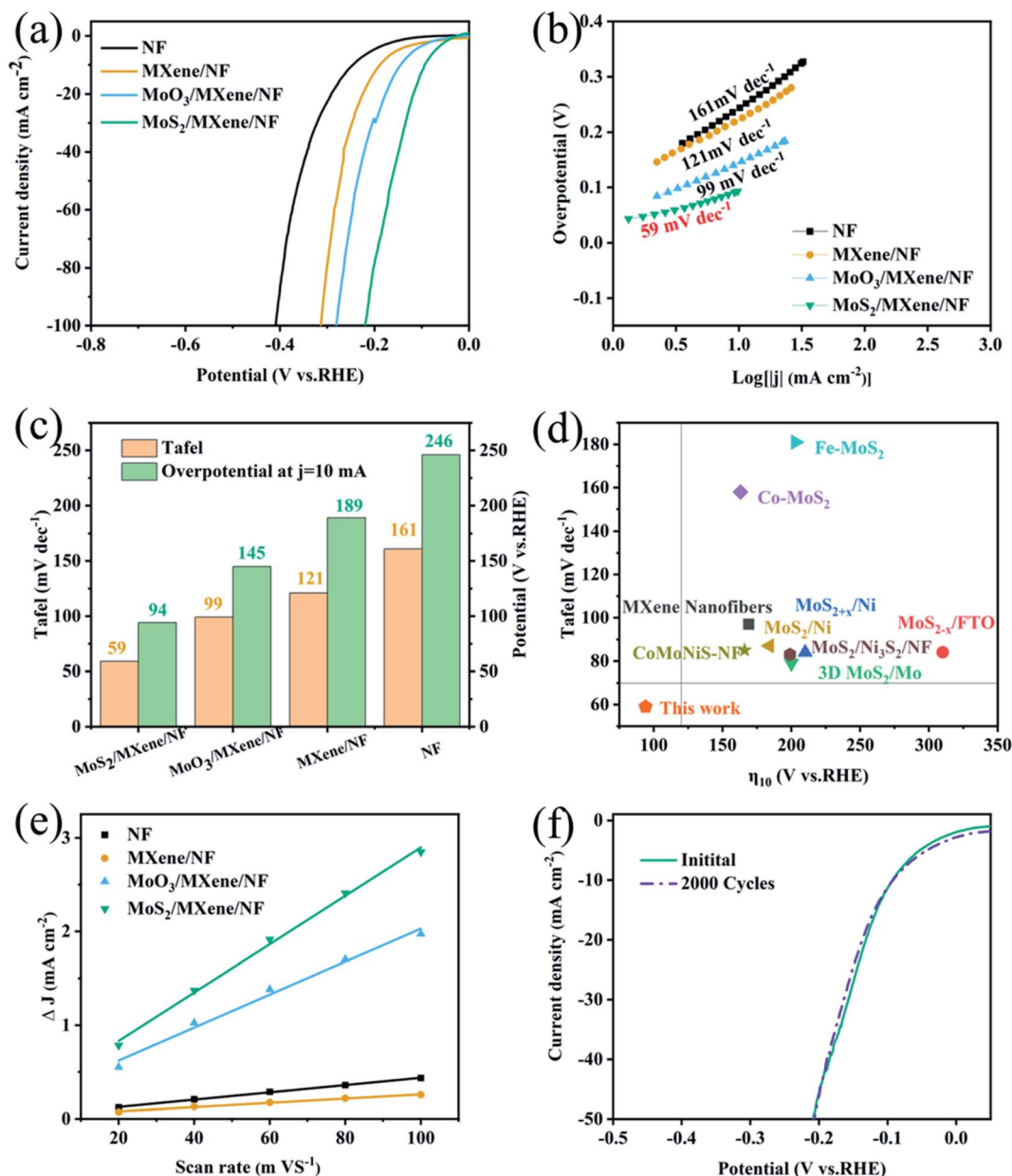
Fig. 4 Electrochemical HER performance. (a) Polarization curves and (b) corresponding Tafel plots of MoS$_2$/MXene/NF, MoO$_3$/MXene/NF, MXene/NF, NF in 1 M KOH. (c) Comparison of overpotentials at 10 mA cm^{-2} (η_{10}) and Tafel slopes for prepared samples. (d) Electrocatalytic activity comparison of MoS$_2$ based materials.[14,23,29,35,38,39] (e) LSV curves of MoS$_2$/MXene/NF before and after 2000 cyclic potential scans. (f) Linear fits of half capacitive currents vs. scan rates for the extraction of C_{dl}.

improve the electrocatalytic performance. Meanwhile, the exposures of MoS$_2$ edges in the outside of interfaces provide active sites for the generation of H*.

The effect of sulfurization temperatures (500 °C and 800 °C) on HER activity was evaluated. The SEM image (Fig. 5a) of MoS$_2$/MXene/NF powder obtained after sulfurization treatment at 500 °C displays negligible change in morphology, and structure, while obvious particles appear in MXene flakes (Fig. 5b), identified as TiO$_2$ (Fig. S10,† JCPDS no. 21-1271) when increasing the sulfurization temperature to 800 °C. As shown in Fig. 5c, the overpotentials for achieving 10 mA cm^{-2} for samples treated at

500 °C and 800 °C are 151 and 128 mV, respectively. Meanwhile, the corresponding Tafel slopes are 128 and 126 mV dec^{-1} (Fig. 5d), respectively. Obviously, the MoS$_2$/MXene/NF treated at 650 °C exhibits the best HER activity among the three samples. The deteriorating HER performance of the MoS$_2$/MXene/NF treated at 800 °C should be attributed to the high temperature induced oxidation of MXene which would reduce the MoS$_2$/MXene conductivity and block the electron transfer channel. The MoS$_2$/MXene/NF treated at low temperature (500 °C) has even poorer intrinsic activity than initial MoO$_3$/MXene/NF (Fig. 4a and b), which may be related to the nanostructure
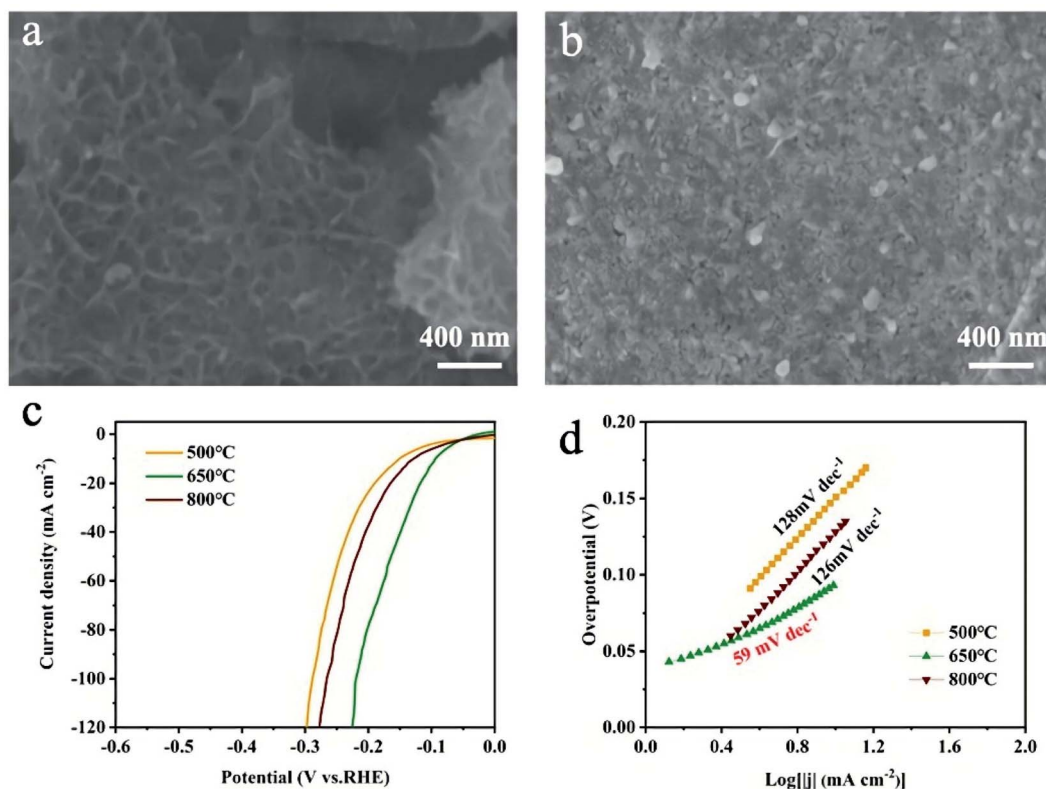
Fig. 5 SEM images of MoS_2/MXene/NF after sulfurization at (a) 500 °C and (b) 800 °C. (c) Polarization curves and (d) corresponding Tafel plots of MoS_2/MXene/NF sulfurized at different temperatures.

destruction of MoO_3 and MoS_2 under insufficient sulfurization. According to the literature,[32,39,40] temperature can control the degree of sulfurization, and molybdenum disulfide is continuously formed on the surface of molybdenum oxide at high temperatures. For the MoO_3/MXene/NF electrode at low temperature, few active sites on the molybdenum disulfide edge can be exposed. And molybdenum oxide is destroyed in the sulfurization process at the same time, so the active sites of the catalyst are greatly reduced. What's more, the alkaline HER process includes two microscopic steps:[41,42] (a) $H_2O + e^- \rightarrow H^* + OH^-$ (Volmer reaction); (2) $H^* + H_2O + e^- \rightarrow H_2 + OH^-$ (Heyrovsky reaction) or $H^* + H^* \rightarrow H_2$ (Tafel reaction). The Tafel slope of MoS_2/MXene/NF (500 °C) is 128 mV dec^{-1} (>120 mV), indicating that the Volmer reaction is the rate-limiting step of the HER due to the deficiency of active sites. The Tafel slope of MoO_3/MXene/NF and MoS_2/MXene/NF (650 °C) declined to 99 and 59 mV dec^{-1}, respectively, implying that the Heyrovsky reaction or Tafel reaction has transited to the rate-determining step. A comparison experiment further indicated that both MXene flakes with higher conductivity and MoS_2 nanodots with more active site exposure are significant to MoS_2/MXene/NF with extraordinary HER performance.

Based on the aforementioned analysis, the remarkable HER activity of MoS_2/MXene/NF (650 °C) is assumed to originate from the following factors: (1) *in situ* polymerized PDA with chelated molybdate ions plays a key role in avoiding $Ti_3C_2T_x$ aggregation and protecting the structure; (2) PDA chelated

MoO_4^{2-} makes the molybdenum compound highly disperse ultrasmall nanostructures on the surface of the MXene flakes; (3) the special heterostructures of MoS_2 nanodots and $Ti_3C_2T_x$ flakes guarantee excellent HER performance and long-term stability; (4) after sulfurization at an appropriate temperature, MoS_2 nanodots grow vertically on $Ti_3C_2T_x$ MXene flakes, accompanied by the high accessibility of active sites for the HER at the MoS_2 nanodot edge; (5) the intense synergistic effect of the MoS_2–$Ti_3C_2T_x$ heterostructure provides a resistance-less channel for faster electron transfer when the active sites of MoS_2 generate H^*.

Conclusion

In summary, a high-activity and high-stability MoS_2/MXene/NF catalyst based on non-precious metal was developed through an *in situ* polymerization strategy and high-temperature sulfurization treatment. The HAADF image and EDX element distribution showed the synthetic MoS_2 anchored on $Ti_3C_2T_x$ MXene flakes with uniformly dispersed ultrasmall nanodots. Electronic microscopies indicated that the constructed MoS_2/MXene heterostructure displayed excellent stability, preventing the aggregation of both the $Ti_3C_2T_x$ flakes and molybdenum compound nanodots, thus providing high accessibility exposure of active sites for the HER. The $Ti_3C_2T_x$ flakes between MoS_2 and NF have multiple functions, which can protect the NF substrate from the sulfurization reaction, increase the stability of the substrate,

and enhance the conductivity of electron transport. The MoS_2 nanodots sulfurized from MoO_3 achieve an exposure of high-activity edges on the (002) plane, providing better HER performance in an alkaline solution. Compared with NF, MXenes, MoO_3, and MoS_2, the prepared MoS_2/MXene/NF exhibited a Tafel slope of 59 mV dec^{-1} and an overpotential of 94 mV at 10 mA cm^{-2}, which is better than those of most of the non-noble metal catalysts in alkaline solution. These findings and insights encourage further heterostructure design and coupling effect investigation of HER catalysts, and point to a new pathway for industrial alkaline catalysis for water splitting.

Author contributions

Xiaoyu Wang: experiments and data collection; Wenbin You: characterization and analysis; Liting Yang, Guanyu Chen, Zhengchen Wu, and Chang Zhang: characterization; Qianjin Chen and Renchao Che: experimental design and project lead. The manuscript was written through contributions of all authors. All authors have given approval to the final version of the manuscript.

Conflicts of interest

The authors declare no conflict of interest.

Acknowledgements

References

1 Z. W. Seh, J. Kibsgaard, C. F. Dickens, I. B. Chorkendorff, J. K. Norskov and T. F. Jaramillo, *Science*, 2017, 355.

2 F. Dawood, M. Anda and G. M. Shafiullah, *Int. J. Hydrogen Energy*, 2020, **45**, 3847–3869.

3 K. T. Moller, T. R. Jensen, E. Akiba and H.-w. Li, *Prog. Nat. Sci.: Mater. Int.*, 2017, **27**, 34–40.

4 I. Roger, M. A. Shipman and M. D. Symes, *Nat. Rev. Chem.*, 2017, **1**, 0003.

5 Y. Yan, B. Y. Xia, B. Zhao and X. Wang, *J. Mater. Chem. A*, 2016, **4**, 17587–17603.

6 B. You, M. T. Tang, C. Tsai, F. Abild-Pedersen, X. Zheng and H. Li, *Adv. Mater.*, 2019, **31**, 1807001.

7 M. Mitov, E. Chorbadzhiyska, R. Rashkov and Y. Hubenova, *Int. J. Hydrogen Energy*, 2012, **37**, 16522–16526.

8 Y. Zheng, Y. Jiao, A. Vasileff and S.-Z. Qiao, *Angew. Chem., Int. Ed.*, 2018, **57**, 7568–7579.

9 S. Ghasemi, S. R. Hosseini and S. Nabipour, *J. Iran. Chem. Soc.*, 2019, **16**, 101–109.

10 Z. Wu, Z. Yang, C. Jin, Y. Zhao and R. Che, *ACS Appl. Mater. Interfaces*, 2021, **13**, 5866–5876.

11 Q. Ding, B. Song, P. Xu and S. Jin, *Chem*, 2016, **1**, 699–726.

12 X. Geng, W. Wu, N. Li, W. Sun, J. Armstrong, A. Al-hilo, M. Brozak, J. Cui and T.-p. Chen, *Adv. Funct. Mater.*, 2014, **24**, 6123–6129.

13 M. I. A. A. Maksoud, A. G. Bedir, M. Bekhit, M. M. Abouelela, R. A. Fahim, A. S. Awed, S. Y. Attia, S. M. Kassem, M. Abd Elkodous, G. S. El-Sayyad, S. G. Mohamed, A. I. Osman, A. a. H. Al-Muhtaseb and D. W. Rooney, *Environ. Chem. Lett.*, 2021, **19**, 3645–3681.

14 Y. Yang, H. Yao, Z. Yu, S. M. Islam, H. He, M. Yuan, Y. Yue, K. Xu, W. Hao, G. Sun, H. Li, S. Ma, P. Zapol and M. G. Kanatzidis, *J. Am. Chem. Soc.*, 2019, **141**, 10417–10430.

15 H. Wang, X. Xiao, S. Liu, C.-L. Chiang, X. Kuai, C.-K. Peng, Y.-C. Lin, X. Meng, J. Zhao, J. Choi, Y.-G. Lin, J.-M. Lee and L. Gao, *J. Am. Chem. Soc.*, 2019, **141**, 18578–18584.

16 J. Hu, C. Zhang, L. Jiang, H. Lin, Y. An, D. Zhou, M. K. H. Leung and S. Yang, *Joule*, 2017, **1**, 383–393.

17 T. F. Jaramillo, K. P. Jorgensen, J. Bonde, J. H. Nielsen, S. Horch and I. Chorkendorff, *Science*, 2007, **317**, 100–102.

18 B. Hinnemann, P. G. Moses, J. Bonde, K. P. Jorgensen, J. H. Nielsen, S. Horch, I. Chorkendorff and J. K. Norskov, *J. Am. Chem. Soc.*, 2005, **127**, 5308–5309.

19 D. Voiry, R. Fullon, J. Yang, C. d. C. Castro e Silva, R. Kappera, I. Bozkurt, D. Kaplan, M. J. Lagos, P. E. Batson, G. Gupta, A. D. Mohite, L. Dong, D. Er, V. B. Shenoy, T. Asefa and M. Chhowalla, *Nat. Mater.*, 2016, **15**, 1003–1009.

20 B. Zhang, J. Liu, J. Wang, Y. Ruan, X. Ji, K. Xu, C. Chen, H. Wan, L. Miao and J. Jiang, *Nano Energy*, 2017, **37**, 74–80.

21 G. Zhao, P. Li, K. Rui, Y. Chen, S. X. Dou and W. Sun, *Chem.–Eur. J.*, 2018, **24**, 11158–11165.

22 G. Ou, P. Fan, X. Ke, Y. Xu, K. Huang, H. Wei, W. Yu, H. Zhang, M. Zhong, H. Wu and Y. Li, *Nano Res.*, 2018, **11**, 751–761.

23 J. Zhang, T. Wang, P. Liu, S. Liu, R. Dong, X. Zhuang, M. Chen and X. Feng, *Energy Environ. Sci.*, 2016, **9**, 2789–2793.

24 S. Xu, D. Li and P. Wu, *Adv. Funct. Mater.*, 2015, **25**, 1127–1136.

25 S. Anantharaj, S. Noda, V. R. Jothi, S. Yi, M. Driess and P. W. Menezes, *Angew. Chem., Int. Ed.*, 2021, **60**, 18981–19006.

26 X. Wang, Y. Zheng, W. Sheng, Z. J. Xu, M. Jaroniec and S.-Z. Qiao, *Mater. Today*, 2020, **36**, 125–138.

27 J. Lin, P. Wang, H. Wang, C. Li, X. Si, J. Qi, J. Cao, Z. Zhong, W. Fei and J. Feng, *Adv. Sci.*, 2019, **6**, 1900246.

28 X. Li, W. You, L. Wang, J. Liu, Z. Wu, K. Pei, Y. Li and R. Che, *ACS Appl. Mater. Interfaces*, 2019, **11**, 44536–44544.

29 J. Zhang, T. Wang, D. Pohl, B. Rellinghaus, R. Dong, S. Liu, X. Zhuang and X. Feng, *Angew. Chem., Int. Ed.*, 2016, **55**, 6702–6707.

30 H. Huang, J. Cui, G. Liu, R. Bi and L. Zhang, *ACS Nano*, 2019, **13**, 3448–3456.

31 Y. Wei, R. A. Soomro, X. Xie and B. Xu, *J. Energy Chem.*, 2021, **55**, 244–255.

32 H. Wang, Y. Lin, S. Liu, J. Li, L. Bu, J. Chen, X. Xiao, J.-H. Choi, L. Gao and J.-M. Lee, *J. Mater. Chem. A*, 2020, **8**, 7109–7116.

33 X. Li, X. Lv, X. Sun, C. Yang, Y.-Z. Zheng, L. Yang, S. Li and X. Tao, *Appl. Catal., B*, 2021, **284**, 119708.

34 J. Liu, Y. Liu, D. Xu, Y. Zhu, W. Peng, Y. Li, F. Zhang and X. Fan, *Appl. Catal., B*, 2019, **241**, 89–94.

35 W. Yuan, L. Cheng, Y. An, H. Wu, N. Yao, X. Fan and X. Guo, *ACS Sustainable Chem. Eng.*, 2018, **6**, 8976–8982.

36 X. Zhan, C. Si, J. Zhou and Z. Sun, *Nanoscale Horiz.*, 2020, **5**, 235–258.

37 S. Seyedin, E. R. S. Yanza and J. M. Razal, *J. Mater. Chem. A*, 2017, **5**, 24076–24082.

38 C. G. Morales-Guio, L. Liardet, M. T. Mayer, S. D. Tilley, M. Graetzel and X. Hu, *Angew. Chem., Int. Ed.*, 2015, **54**, 664–667.

39 B. He, L. Chen, M. Jing, M. Zhou, Z. Hou and X. Chen, *Electrochim. Acta*, 2018, **283**, 357–365.

40 H. F. Liu, S. L. Wong and D. Z. Chi, *Chem. Vap. Deposition*, 2015, **21**, 241–259.

41 Q. Hu, Z. Wang, X. Huang, Y. Qin, H. Yang, X. Ren, Q. Zhang, J. Liu and C. He, *Energy Environ. Sci.*, 2020, **13**, 5097–5103.

42 X. Liu, Q. Hu, B. Zhu, G. Li, L. Fan, X. Chai, Q. Zhang, J. Liu and C. He, *Small*, 2018, **14**, 1802755.